Improved Deadbeat Predictive Current Control With Extended State Observer for Dual Three-Phase PMSMs

Xiaodong Sun, *Senior Member, IEEE*, Xuwei Lin, *Graduate Student Member, IEEE*, Dong Guo, Gang Lei, *Senior Member, IEEE*, and Ming Yao

***Abstract*—A deadbeat predictive current control (DPCC) method based on extended state observer (ESO) is proposed to improve the control performance of dual three-phase permanent magnet synchronous motors (DTP-PMSMs) under parameter mismatch. A variable gain coefficient related to the exponential function of tracking error is proposed to enhance the observer's convergence and robustness under complex conditions. Furthermore, the prediction delay problem of DPCC model under digital hardware is studied, and an improved prediction method is proposed to compensate for the delay time, reducing the response time and overshoot of the system under the DPCC algorithm. The proposed ESO is combined with the improved prediction model, and DPCC with two-sample delays is employed to reduce the prediction current error and enhance the control performance of the algorithm in practical applications. The stability of the system is demonstrated using the Hurwitz Criterion. Experimental results validate the superiority and feasibility of the proposed algorithm for the control and drive of DTP-PMSMs.**

***Index Terms*—Deadbeat predictive current control, dual three-phase permanent magnet synchronous motors (DTP-PMSMs), extended state observer (ESO), parameter mismatch.**

Manuscript received 27 November 2023; revised 30 January 2024; accepted 23 February 2024. Date of publication 27 February 2024; date of current version 19 April 2024. This work was supported in part by the Key Research and Development Program of Jiangsu Province under Grant BE2023052, in part by the Opening Foundation of International Joint Laboratory of Intelligent Manufacturing & Control of Key Parts for Energy-Efficient & New Energy Vehicles, Ministry of Education, under Grant 2023IJLIMC04, and in part by the Opening Foundation of Key Laboratory of Advanced Manufacture Technology for Automobile Parts, Ministry of Education, under Grant 2022 KLMT02. Recommended for publication by Associate Editor R. Kennel. *(Corresponding author: Ming Yao.)*

Xiaodong Sun and Xuwei Lin are with the Automotive Engineering Research Institute, Jiangsu University, Zhenjiang 212013, China (e-mail: xdsun@ujs.edu.cn; 2222204043@stmail.ujs.edu.cn).

Dong Guo is with the International Joint Laboratory of Intelligent Manufacturing & Control of Key Parts for Energy-efficient & New Energy Vehicles, Ministry of Education, Chongqing University of Technology, Chongqing 400054, China, and also with the School of Vehicle Engineering, Chongqing University of Technology, Chongqing 400054, China (e-mail: guodong@cqut.edu.cn).

Gang Lei is with the School of Electrical and Data Engineering, University of Technology Sydney, Ultimo, NSW 2007, Australia (e-mail: gang.lei@uts.edu.au).

Ming Yao is with the School of Automotive and Traffic Engineering, Jiangsu University, Zhenjiang 212013, China (e-mail: ymluck@ujs.edu.cn).

Color versions of one or more figures in this article are available at https://doi.org/10.1109/TPEL.2024.3370622.

Digital Object Identifier 10.1109/TPEL.2024.3370622

I. Introduction

DUE to the positive characteristics of high power factor, high operating efficiency and strong stability, permanent magnet synchronous motors (PMSMs) and their speed-regulating drive systems are widely used in ac electric transmission [1], [2], [3]. In recent years, the demand for high-speed drive power has increased in various applications, such as metallurgical rolling, mine lifting, locomotive traction, and marine propulsion [4], [5], [6]. However, due to the limitations of the voltage and current tolerances of power switch devices, it has become challenging to meet industrial needs by simply increasing the current and voltage of three-phase PMSMs [7], [8]. One way to realize high-power transmission is to increase the number of motor phases and reduce the requirement of phase capacity of the inverter [9]. Since the broad application of power electronic frequency converter, motor drives can be completely free from the restrictions of a three-phase power supply system. Polyphase inverter power supplies can also achieve high-power ac transmission [10].

In power electronics and electrical drives, dual three-phase permanent magnet synchronous motors (DTP-PMSMs) have aroused extensive interest in engineering and academic circles because of their high reliability [11], [12]. In the application of motor drive systems, DTP-PMSMs can satisfy the demands of high power efficiency and wide range of load variation. In many applications like electric vehicles, DTP-PMSMs have become the best application choice [13], [14].

Although DTP-PMSMs offer several advantages, their application is often limited by problems such as excessive harmonic current. Therefore, an appropriate control strategy is critical to applying polyphase motors. In recent years, the predictive control method has become a new research hotspot due to its advantages of low accuracy, strong robustness, and stability [15], [16], [17]. In theory, deadbeat control eliminates the hysteresis of conventional PI controllers and enhances motor control precision [18]. In [19], the use of virtual voltage vectors (VVVs) simplifies the calculation of deadbeat flux linkage predictive control, and greatly reduces the harmonics of DTP motors in the z_1-z_2 subspace. In [20], a DPCC with closed error compensation was designed, which eliminates the steady-state error through feedforward compensation of the voltage vector and further suppresses the noise impact the control system receives. In

[21], a new multilevel inverter was introduced into deadbeat control, and a fault-tolerant scheme was designed in case of switch failure, which significantly improved the robustness and reliability of the motor during operation and accelerated the response of tracking current. In [22], the prediction model of the speed loop was improved and combined with a robust cascaded deadbeat predictive speed control method to reduce the delay problem in the speed loop by directly compensating the torque.

However, the performance of deadbeat predictive control largely relies on the accurate mathematical model. In industrial applications, disturbance during motor operation is unavoidable, so the methods to improve robustness of the deadbeat control have been analyzed as one of the concerns of many researchers [23], [24], [25]. In recent years, the strategies based on disturbance observer have been considered as an effective means to improve the systems' robustness [26], [27], [28]. In [29], a composite observer combining the advantages of generalized proportional integral observer (GPIO) and sliding mode observation (SMO) was designed, and introduced into the DPCC control algorithm to reduce the impact of parameter mismatch by reducing the overshoot and settling time when the parameters change. In [30], the deadbeat algorithm was used to predict the harmonic current in the DTP motor, and the linear disturbance observer (LDO) was used to compensate the harmonic plane to avoid the internal and external interference of the motor, thus suppressing the fifth and seventh harmonic problems. In [31], corresponding observers were designed for parameter change and load disturbance. The lumped disturbance was directly estimated and compensated to the current loop by paralleling the feedback loop to obtain higher control accuracy and robustness.

Compared to other observers, extended state observer (ESO) has been widely concerned for its advantages of simple structure and strong robustness [32], [33], [34]. In [35], an active disturbance rejection strategy based on DPCC was proposed, and the optimization and application of liner extend state observer (LESO) greatly improved the robustness of the system. However, the response speed of the strategy under extreme disturbance needs to be further improved. To improve the antidisturbance ability of the prediction system, Wang et al. [36] designed an ESO based on the improved finite element discrete model, which greatly improved the estimation accuracy of disturbance during the transient period. But the enormous computational burden of the strategy cannot be ignored. Compared with LESO, the adaptive extended state observer (AESO) can adjust the observer gain according to different system conditions and improve the noise suppression performance of the system at high gain while maintaining the antidisturbance ability [37], [38]. Therefore, it is increasingly applied in predictive control strategies. By adding an integral term to the system, Wang et al. [39] further improved the accuracy of AESO disturbance compensation in the low gain state. Meanwhile, an inductance parameter estimation method was proposed to update the initial inductance value and reduce the calculation burden of the observer. However, the strategy ignores the inherent delay in the system and cannot cope with the more complex and changeable working conditions. In addition, model-aid extended state observer (MAESO), multifrequency ESO (MF-ESO), and quasi-resonant extended state observer (QRESO) are also proposed to further improve the immunity of DPCC systems [40], [41], [42]. Although the performance of ESO in the control system has been greatly improved after continuous research, more effective strategies still need to be explored in terms of robustness, dynamic response, static performance, etc.

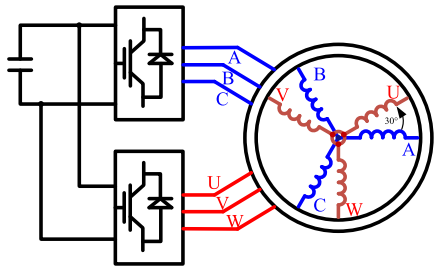

Fig. 1. Structure of DTP-PMSM drives.

This article proposes an improved DPCC control system considering parameter mismatch and inherent delay to improve the operation performance and robustness of DTP-PMSM control under parameter mismatch. An ESO is designed to compensate for the current loop, which takes the control error caused by parameter changes as a lumped disturbance.

The main contributions of this article are as follows.

1) Aiming at the parameter mismatch problem of DTP-PMSM under complex working conditions, a variable gain ESO is designed, which has faster estimation speed and better robustness performance.
2) The prediction model is further optimized for the delay in conventional DPCC. By compensating the lumped delay time, the delay caused by inductance, sensor, and other factors is eliminated.
3) The DPCC strategy based on variable gain ESO is applied to the main subspace and harmonic subspace simultaneously, which improves the robustness while reducing the influence of fifth and seventh harmonic currents.

The rest of this article is structured as follows. The mathematical model of the DTP-PMSM is established in Section II. The conventional deadbeat current control and its parameter sensitivity are analyzed in Section III. The proposed control strategy of DPCC for DTP-PMSM combined with ESO is introduced in Section IV. The control performance of the proposed algorithm is evaluated by experiment in Section V. Finally, Section VI concludes the article.

II. Mathematical Model of DTP-PMSM

As shown in Fig. 1, a DTP-PMSM drive consists of two sets of Y-connected three-phase symmetrical windings, which differ by 30° electrical angles in space. In the natural coordinate system, the voltage equation of the DTP-PMSM can be expressed as (1), and the flux equation can be defined as

$$u_s = R_s i_s + \frac{d\psi_s}{dt} \tag{1}$$

$$\psi_s = L_s i_s + \lambda_s \psi_f \tag{2}$$

where u_s, i_s, ψ_s are stator phase voltage, stator phase current, and stator flux, respectively. R_s and L_s are the resistance and inductance, respectively. λ_s is the flux coefficient, and ψ_f is the flux amplitude generated by the permanent magnet in each phase winding.

In order to fully embody the multifreedom of DTP-PMSM, the vector space decomposition (VSD) method is adopted. Through VSD coordinate transformation, each variable of the motor will be mapped to three orthogonal subspaces, respectively, α-β subspace, z_1-z_2 subspace, and o_1-o_2 subspace.

The idea model under synchronous rotating coordinates obtained by VSD can be expressed as

$$\begin{bmatrix} u_d \\ u_q \\ u_{z_1} \\ u_{z_2} \end{bmatrix} = \begin{bmatrix} R_s & 0 & 0 & 0 \\ 0 & R_s & 0 & 0 \\ 0 & 0 & R_s & 0 \\ 0 & 0 & 0 & R_s \end{bmatrix} \begin{bmatrix} i_d \\ i_q \\ i_{z_1} \\ i_{z_2} \end{bmatrix} + \begin{bmatrix} \dot{\psi}_d \\ \dot{\psi}_q \\ \dot{\psi}_{z_1} \\ \dot{\psi}_{z_1} \end{bmatrix} + \omega_e \begin{bmatrix} -\psi_q \\ \psi_d \\ 0 \\ 0 \end{bmatrix} \tag{3}$$

$$\begin{bmatrix} \psi_d \\ \psi_q \\ \psi_{z_1} \\ \psi_{z_2} \end{bmatrix} = \begin{bmatrix} L_d & 0 & 0 & 0 \\ 0 & L_q & 0 & 0 \\ 0 & 0 & L_z & 0 \\ 0 & 0 & 0 & L_z \end{bmatrix} \begin{bmatrix} i_d \\ i_q \\ i_{z_1} \\ i_{z_2} \end{bmatrix} + \begin{bmatrix} 1 \\ 0 \\ 0 \\ 0 \end{bmatrix} \psi_f \tag{4}$$

$$T_e = 3p_n \left[\left(L_d - L_q \right) i_d i_q + i_q \psi_f \right] \tag{5}$$

where L_z is the leakage inductance, ω_e is the electric angular speed of the rotor, T_e is the electromagnetic torque, and p_n is the number of pole pairs. Subscripts "dq" and "z_1z_2" denote the voltage, current, inductance, and flux in d-q subspace and z_1-z_2 subspace, respectively.

In order to improve the performance of the conventional vector control, an improved deadbeat predictive current control is also used for z_1-z_2 subspace in this article.

III. Conventional Deadbeat Current Control and Parameter Sensitivity Analysis

A. Conventional Control Method

Conventional DPCC relies on precise discretized models of PMSM. Since the current loop's sampling period (Ts) is usually very small, the zero-order hold method is used to discretize the model. Combined with (3) and (4), the equivalent discretization model of DTP-PMSM can be expressed as

$$\begin{bmatrix} i_d(k+1) \\ i_q(k+1) \\ i_{z_1}(k+1) \\ i_{z_2}(k+1) \end{bmatrix} = \boldsymbol{E}(k) \begin{bmatrix} i_d(k) \\ i_q(k) \\ i_{z_1}(k) \\ i_{z_2}(k) \end{bmatrix} + \boldsymbol{F} \begin{bmatrix} u_d(k) \\ u_q(k) \\ u_{z_1}(k) \\ u_{z_2}(k) \end{bmatrix} + \boldsymbol{M}(k) \tag{6}$$

where $\boldsymbol{M}(k) = [0\ -\omega_e(k)\psi_f/L_q\ 0\ 0]^{\mathrm{T}}$, $\boldsymbol{F} = \mathrm{diag}[1/L_d\ 1/L_q\ 1/L_{xy}\ 1/L_{xy}]$

$$\boldsymbol{E}(k) = \begin{bmatrix} 1 - \frac{R_s T_s}{L_d} & \omega_e(k) \frac{L_q T_s}{L_d} & 0 & 0 \\ -\omega_e(k) \frac{L_d T_s}{L_q} & 1 - \frac{R_s T_s}{L_q} & 0 & 0 \\ 0 & 0 & 1 - \frac{R_s T_s}{L_z} & 0 \\ 0 & 0 & 0 & 1 - \frac{R_s T_s}{L_z} \end{bmatrix}.$$

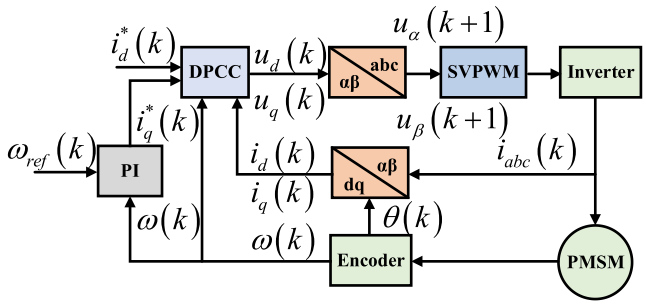

Fig. 2. Control diagram of conventional DPCC.

As shown in Fig. 2, the predicted voltage and their duty cycle ratio are calculated in k control cycles. Limited by hardware conditions, the microprocessor can only update the duty cycle ratio until the initial time of $k+1$ control cycles. The predicted voltages can then be applied to the motor via SVPWM.

However, the actual current of the motor has been changed. This will lead to inaccurate predictions of the reference voltage. To eliminate the influence of sampling delay, the states at the $k+1$ instant and $k+2$ instant will be selected to calculate reference voltage at the instant of k, which can be expressed as

$$\begin{bmatrix} u_d^* \\ u_q^* \\ u_{z_1}^* \\ u_{z_2}^* \end{bmatrix} = \boldsymbol{F}^{-1} \left\{ \begin{bmatrix} i_d(k+2) \\ i_q(k+2) \\ i_{z_1}(k+2) \\ i_{z_2}(k+2) \end{bmatrix} - \boldsymbol{E}(k+1) \begin{bmatrix} i_d(k+1) \\ i_q(k+1) \\ i_{z_1}(k+1) \\ i_{z_2}(k+1) \end{bmatrix} - \boldsymbol{M}(k+1) \right\} \tag{7}$$

where the current at time $k+2$ is replaced by the reference current. The current at $k+1$ instant cannot be directly obtained and needs to be predicted at the instant of k, as given by

$$\begin{bmatrix} i_d(k+1) \\ i_q(k+1) \\ i_{z_1}(k+1) \\ i_{z_2}(k+1) \end{bmatrix} = \boldsymbol{E}(k) \begin{bmatrix} i_d(k) \\ i_q(k) \\ i_{z_1}(k) \\ i_{z_2}(k) \end{bmatrix} + \boldsymbol{F} \begin{bmatrix} u_d^*(k-1) \\ u_q^*(k-1) \\ u_{z_1}^*(k-1) \\ u_{z_2}^*(k-1) \end{bmatrix} + \boldsymbol{M}(k). \tag{8}$$

By combining (7) and (8), the reference voltage of DPCC, considering two sampling delays, can be obtained.

B. Parameter Sensitivity Analysis on DPCC

As a predictive control algorithm based on the discrete model, the DPCC greatly depends on the accuracy of the motor mathematical model. In practical application, temperature, load, and other factors will cause mismatches for L_s, R_s, and ψ_f, compared with their calibrated values, thus further affecting the control effectiveness. To further determine the impact of parameter mismatch, the parameter sensitivity of DPCC is analyzed in detail in this section.

Since the consequences caused by parameter mismatch mainly affect the d-q subspace, the analysis in this section primarily concentrates on the d-q subspace.

According to (7), the ideal discrete current prediction model of DTP-PMSM in d-q subspace can be represented as

$$\begin{bmatrix} i_d^{ref}(k+2) \\ i_q^{ref}(k+2) \end{bmatrix} = \boldsymbol{E}_{dq}(k+1)\begin{bmatrix} i_d(k+1) \\ i_q(k+1) \end{bmatrix} + \boldsymbol{F}_{dq}\begin{bmatrix} u_d^*(k) \\ u^*{}_q(k) \end{bmatrix} + \boldsymbol{M}_{dq}(k+1) \tag{9}$$

where $\boldsymbol{E}_{dq}(k) = \begin{bmatrix} 1-\frac{R_sT_s}{L_d} & \omega_e(k)T_s\frac{L_q}{L_d} \\ -\omega_e(k)T_s\frac{L_d}{L_q} & 1-\frac{R_sT_s}{L_q} \end{bmatrix}$ $\boldsymbol{F}_{dq} = \begin{bmatrix} \frac{T_s}{L_d} & 0 \\ 0 & \frac{T_s}{L_q} \end{bmatrix}$ $\boldsymbol{M}_{dq}(k) = \begin{bmatrix} 0 \\ -\frac{\omega_e(k)\psi_f T_s}{L_q} \end{bmatrix}$ ${i_d}^{ref}(k+2)$ and ${i_q}^{ref}(k+2)$ are the reference currents. The actual current prediction model considering disturbance can be expressed as

$$\begin{bmatrix} i_d(k+2) \\ i_q(k+2) \end{bmatrix} = \tilde{\boldsymbol{E}}_{dq}(k+1)\begin{bmatrix} i_d(k+1) \\ i_q(k+1) \end{bmatrix} + \tilde{\boldsymbol{F}}_{dq}\begin{bmatrix} u_d(k) \\ u_q(k) \end{bmatrix} + \tilde{\boldsymbol{M}}_{dq}(k+1) \tag{10}$$

where

$$\tilde{\boldsymbol{E}}_{dq}(k) = \begin{bmatrix} 1-\frac{\tilde{R}_sT_s}{\tilde{L}_d} & \omega_e(k)T_s\frac{\tilde{L}_q}{\tilde{L}_d} \\ -\omega_e(k)T_s\frac{\tilde{L}_d}{\tilde{L}_q} & 1-\frac{\tilde{R}_sT_s}{\tilde{L}_q} \end{bmatrix}; \tilde{\boldsymbol{F}}_{dq} = \begin{bmatrix} \frac{T_s}{\tilde{L}_d} & 0 \\ 0 & \frac{T_s}{\tilde{L}_q} \end{bmatrix};$$

$$\tilde{\boldsymbol{M}}_{dq}(k) = \begin{bmatrix} 0 \\ -\frac{\omega_e(k)\tilde{\psi}_f T_s}{\tilde{L}_q} \end{bmatrix}.$$

$\tilde{R}_s = R_s + \Delta R_s$, $\tilde{L}_{dq} = L_{dq} + \Delta L_{dq}$, $\tilde{\psi}_f = \psi_f + \Delta\psi_f$, $\Delta R_s, \Delta L_{dq}, \Delta\psi_f$ are the difference between the actual and calibrated values of stator resistance, inductance, and flux linkage, respectively.

According to (9) and (10), steady-state error will exist when the parameters of DTP-PMSM are mismatched, and the actual current loses the tracking ability to reference current. The error can be expressed as

$$\begin{bmatrix} i_d^{ref}(k+2) \\ i_q^{ref}(k+2) \end{bmatrix} = \begin{bmatrix} i_d(k+2) \\ i_q(k+2) \end{bmatrix} + \begin{bmatrix} e_d(k) \\ e_q(k) \end{bmatrix} \tag{11}$$

$$\begin{cases} e_d(k) = i_d^{ref}(k+2) - i_d(k+2) \\ \quad = -H_dT_si_d(k+1) + J_dT_s\omega_e i_q(k+1) \\ \quad +R_dT_su_d(k) \\ e_q(k) = i_q^{ref}(k+2) - i_q(k+2) \\ \quad = -H_qT_si_q(k+1) + J_qT_s\omega_e i_d(k+1) \\ \quad +R_qT_su_q(k) \\ \quad -\frac{\psi_f\Delta L_q - L_q\Delta\psi_f}{L_q(L_q+\Delta L_q)}T_s\omega_e \end{cases} \tag{12}$$

where

$$H_d = \frac{R_s\Delta L_d - \Delta R_sL_d}{L_d(L_d+\Delta L_d)} H_q = \frac{R_s\Delta L_q - \Delta R_sL_q}{L_q(L_q+\Delta L_q)}$$

$$J_d = \frac{L_q\Delta L_d - L_d\Delta L_q}{L_d(L_d+\Delta L_d)} J_q = \frac{L_q\Delta L_d - L_d\Delta L_q}{L_d(L_d+\Delta L_d)}$$

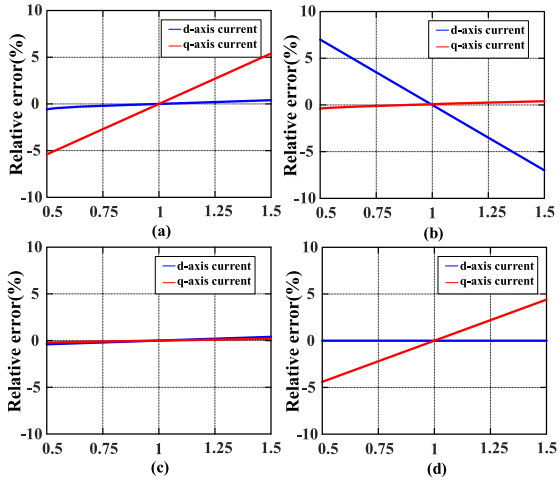

Fig. 3. Relative errors of dq-axis currents when the value of each parameter changes from 0.5 times of the calibration value to 1.5 times. (a) Errors of d-axis inductance variation. (b) Errors of q-axis inductance variation. (c) Errors of stator resistance variation. (d) Errors of flux linkage variation.

TABLE I
PARAMETERS OF THE DTP-PMSM

Parameter	Symbol	Value
No. of pole pairs	P	22
Stator resistance	R_s	4.5 Ω
d-axis inductance	L_d	25 mH
q-axis inductance	L_q	35 mH
Leakage inductance	L_z	8 mH
Flux linkage of magnet	ψ_f	0.25 Wb
Inertia	J	0.0015 kg.m^2
Rated speed	n	500 r/min
Rated power	P_N	30 kW

$$R_d = \frac{\Delta L_d}{L_d(L_d+\Delta L_d)} R_q = \frac{\Delta L_q}{L_q(L_q+\Delta L_q)}.$$

Fig. 3 shows the relationship between the steady-state error of the current response and inductance L_d, L_q, resistance R_s, and flux linkage ψ_f when the motor parameter mismatches at the reference speed of 400 r/min, and the reference current of 10 A. The main parameters of the DTP-PMSM are listed in Table I in Section V.

According to Fig. 3(a) and (b), both d-axis and q-axis currents are significantly affected in the case of mismatched inductance L_d and L_q. As shown in Fig. 3(c), when the sampling time is sufficiently small, the minimal error that occurs by the stator resistance mismatch can be ignored. While inaccurate flux linkage will not affect the d-axis current, it will cause a large q-axis current prediction error.

To improve the control performance of DPCC under parameter variation, an ESO is designed to enhance the robustness of the predictive current controller.

IV. DPCC With Extended State Observer

A. Proposed Extended State Observer

Due to the effect caused by parameter mismatch and other factors, the current dynamic model of DTP-PMSM can be

expressed as (13). Considering that the z_1-z_2 plane is similar to the d-q plane, the analysis is only conducted in the d-q plane for ease of calculation in this article

$$\dot{x} = \tilde{\boldsymbol{A}}x + \tilde{\boldsymbol{B}}u + \tilde{\boldsymbol{G}} \tag{13}$$

where $x = [i_d\ i_q]^{\mathrm{T}}$, $u = [u_d\ u_q]^{\mathrm{T}}$

$$\tilde{\boldsymbol{A}} = \begin{bmatrix} 1 - \frac{\tilde{R}_s}{\tilde{L}_d} & \omega_e \frac{\tilde{L}_q}{\tilde{L}_d} \\ -\omega_e \frac{\tilde{L}_d}{\tilde{L}_q} & 1 - \frac{\tilde{R}_s}{\tilde{L}_q} \end{bmatrix}; \tilde{\boldsymbol{G}} = \begin{bmatrix} 0 \\ -\frac{\omega_e \tilde{\psi}_f}{\tilde{L}_q} \end{bmatrix}; \tilde{\boldsymbol{B}} = \begin{bmatrix} \frac{1}{\tilde{L}_d} & 0 \\ 0 & \frac{1}{\tilde{L}_q} \end{bmatrix}.$$

In order to express the error caused by parameter mismatch in the form of lumped disturbance, (13) can be further expressed as

$$\begin{aligned} \dot{x} &= \tilde{\boldsymbol{A}}x + \tilde{\boldsymbol{B}}u + \tilde{\boldsymbol{G}} \\ &= \boldsymbol{A}x + \boldsymbol{B}u + \left(\tilde{\boldsymbol{A}} - \boldsymbol{A}\right)x + \left(\tilde{\boldsymbol{B}} - \boldsymbol{B}\right)u + \tilde{\boldsymbol{G}} \\ &= \boldsymbol{A}x + \boldsymbol{B}u + \boldsymbol{d} \end{aligned} \tag{14}$$

where $\boldsymbol{d}$ is the lumped disturbance, and represents the error caused by parameter mismatch.

Since the concentrated disturbance cannot be directly measured in practice, d is regarded as an extended state variable, and the state-space equation can be expressed as

$$\begin{aligned} \dot{x} &= \boldsymbol{A}x + d + \boldsymbol{B}u \\ \dot{d} &= F_d \end{aligned} \tag{15}$$

where F_d is the variation rate of d.

F_d can be discretized as

$$F_d(k) = \frac{d(k+1) - d(k)}{T_s}. \tag{16}$$

It is worth mentioning that the changes of current ΔI_{dq} and lumped disturbance Δd are actually limited in a sampling period due to the limitation of space voltage and leakage inductance. Therefore, combined with (16), the rate of change of the disturbance F_d can also be assumed to be bounded in this article.

It can be seen from (15) that the current state-space equation of DTP-PMSM conforms to the standard form of the first-order extended state observer. Thus, the ESO can be designed as follows:

$$\begin{cases} \dot{\breve{\hat{x}}} = \breve{\boldsymbol{A}}\breve{\hat{x}} + \breve{\boldsymbol{B}}u + \boldsymbol{L}\breve{\boldsymbol{C}}\left(\breve{x} - \breve{\hat{x}}\right) \\ \breve{\hat{y}} = \breve{\boldsymbol{C}}\breve{\hat{x}} \end{cases} \tag{17}$$

where $\breve{x} = [x \quad d]^T$, $\breve{\hat{x}} = [\hat{x} \quad \hat{d}]^T$. $\hat{x}$ and $\hat{d}$ are the observed values of x and d, respectively. $\boldsymbol{L}$ is the feedback matrix. $\breve{\hat{y}}$ is the output of the observer and

$$\breve{\boldsymbol{A}} = \begin{bmatrix} \boldsymbol{A} & \boldsymbol{I} \\ 0 & 0 \end{bmatrix}; \breve{\boldsymbol{B}} = \begin{bmatrix} \boldsymbol{B} \\ 0 \end{bmatrix}; \breve{\boldsymbol{C}} = \begin{bmatrix} C & 0 \end{bmatrix}.$$

In this article, $c = 1$. By designing a compensation matrix, lumped disturbance and its rate of variation can be estimated by ESO.

ESO gets an estimate of the current and lumped disturbance through $\breve{\hat{x}}$. The observed current replaces the original current feedback value to participate in the closed-loop control, and the observed disturbance $\hat{d}$ acts as feedforward compensation to eliminate the influence caused by parameter disturbance.

In order to study the selection of the feedback matrix L, according to (17), the eigenvalue of the observer can be obtained through

$$\left|s\boldsymbol{I} - \left(\breve{\boldsymbol{A}} - \boldsymbol{L}\breve{\boldsymbol{C}}\right)\right| = \prod_{i=1}^{n}(s - \lambda_i) \tag{18}$$

where n is the dimension of $\breve{\hat{x}}$ and λ_i is the eigenvalue.

It can be seen from (18) that the selection of the feedback matrix L determines the position of the eigenvalues and poles on the complex plane. The assignment of eigenvalues is studied below to improve the observer's performance in the system. To simplify the calculation, single identical eigenvalues are assigned. Assume

$$\boldsymbol{L} = \begin{bmatrix} l_1 & 0 & l_3 & 0 \\ 0 & l_2 & 0 & l_4 \end{bmatrix}^T \tag{19}$$

where l_1,l_2,l_3,l_4 are positive values.

Combining (18) and (19), the eigenvalues can be expressed as

$$\begin{cases} l_1 = -R_s/L_d - 2\lambda - |\omega_e| \\ l_2 = -R_s/L_q - 2\lambda + |\omega_e| \\ l_3 = l_4 = \lambda^2. \end{cases} \tag{20}$$

To improve the ESO's robustness, a variable gain ESO parameter design method is adopted in this article. The control poles and eigenvalues of the system will vary with the current tracking error. The variable k is determined by the tangent function for the current error and is proportional to the gain of ESO. When a significant difference exists between the actual and estimated values, the variable k is adjusted to enhance the observer eigenvalue and hasten observer convergence. Therefore, it obtains

$$\begin{cases} k = 1 + \tan\left(\zeta\left|x - \hat{x}\right|/M\right), \zeta \in [0, \pi/2] \\ \bar{\lambda}_i = k\lambda_i, i = 1, \ldots, n \end{cases} \tag{21}$$

where ξ is the variable gain coefficient and M is the limit of $|x - \hat{x}|$.

By combining (19)–(21), the ESO expression can be rewritten as

$$\dot{\breve{\hat{x}}} = \breve{\boldsymbol{A}}\breve{\hat{x}} + \breve{\boldsymbol{B}}u + K\boldsymbol{L}\left(\breve{x} - \breve{\hat{x}}\right) \tag{22}$$

where $K = \mathrm{diag}[k \quad k \quad k^2 \quad k^2]$.

The algorithm can be represented in Fig. 4.

B. Discrete ESO Design

The discretized state using the zero-order retention method can be expressed as

$$\breve{\hat{x}}_{[k+1]} = \breve{\hat{x}}_{[k]} + \left(\breve{\boldsymbol{A}}\breve{\hat{x}}_{[k]} + \breve{\boldsymbol{B}}u_{[k]} + K\boldsymbol{L}\breve{\boldsymbol{C}}\left(\breve{x}_{[k]} - \breve{\hat{x}}_{[k]}\right)\right)T_s. \tag{23}$$

In practical applications, the control signal will inevitably be delayed in the hardware transmission, and the input signal $u^r_{[k]}$ obtained by the control system will be different from the

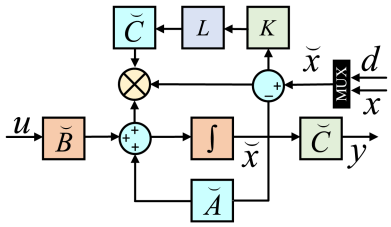

Fig. 4. Diagram of proposed ESO.

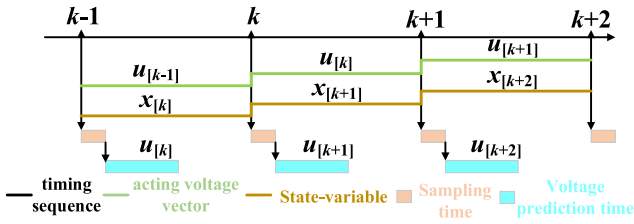

Fig. 5. Control time sequence of DPCC.

actual output signal, resulting in poor current response tracking performance.

According to (23), the actual discretized ESO model can be expressed as

$$\hat{\breve{x}}^{r}_{[k+1]} = \hat{\breve{x}}_{[k]} + \left(\breve{\boldsymbol{A}}\hat{\breve{x}}_{[k]} + \breve{\boldsymbol{B}}u^{r}_{[k]} + K\boldsymbol{L}\breve{\boldsymbol{C}}\left(\breve{x}_{[k]} - \hat{\breve{x}}_{[k]}\right)\right)T_s. \tag{24}$$

Since the actual state of the motor changes when the control voltage predicted by the conventional method is applied, the current response cannot accurately track the reference current all the time. The control indicators, such as overshoot and settling time, are far less than expected. To improve the control performance of the deadbeat system, because the error caused by delay mainly depends on the inertia delay of the system, the improved system can be expressed as

$$\hat{\breve{x}}^{r}_{[k+1]} = \hat{\breve{x}}_{[k]} + \left(\breve{\boldsymbol{A}}\hat{\breve{x}}_{[k]} + \breve{\boldsymbol{B}}u_{[k]} + K\boldsymbol{L}\breve{\boldsymbol{C}}\left(\breve{x}_{[k]} - \hat{\breve{x}}_{[k]}\right)\right)(T_s + hT_s) \tag{25}$$

where hT_s represents lumped delay time. It is mainly composed of inductance delay t_L, current and filter delay t_f, and sensor element delay t_r. It can be expressed as

$$\begin{aligned} hT_s &= t_L + t_f + t_r \\ t_L &= L\Delta i/(u - R_s i - e) \end{aligned} \tag{26}$$

where $\Delta i = i^* - i$ and e is the back electromotive force. In practical application, the delay can be eliminated by adjusting the filter parameters and types, and the influence of t_f can be ignored. Similarly, the delay effect of the sensor element can generally be ignored. Therefore, the system delay time is mainly affected by the inductive delay.

In practical application, the voltage vector, as the input control signal, is given by SVPWM. The control period of DTP-PMSM is derived from the AD module after the current is sampled and interrupted. Therefore, the composition of the delay time in the application is shown in Fig. 5.

To improve control accuracy and eliminate delay error, the DPCC model considering double sampling delay is applied in this article. The voltage vector u_k predicted at the k-1 sampling period is taken as the input to obtain the state variable at the moment $k+1$, to predict the voltage vector applied to the electrode at the next period. Combined with (24) and (25), the proposed DPCC model can be expressed as

$$\hat{\breve{x}}^{r}_{[k+2]} = \hat{\breve{x}}_{[k+1]} + \left(\breve{\boldsymbol{A}}\hat{\breve{x}}_{[k+1]} + \breve{\boldsymbol{B}}u_{[k+1]} + K\boldsymbol{L}\breve{\boldsymbol{C}}\left(\breve{x}_{[k+1]} - \hat{\breve{x}}_{[k+1]}\right)\right)(T_s + hT_s). \tag{27}$$

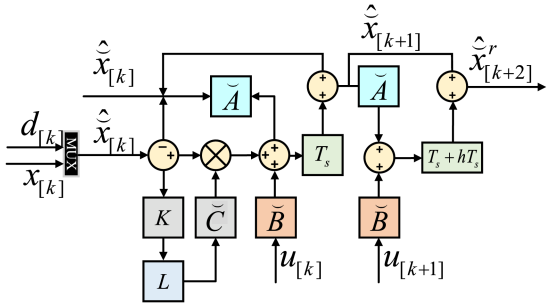

Fig. 6. Diagram of the proposed predicted method.

Since it is difficult to accurately obtain the state variable of the $k+1$ sampling period at the $k+1$ sampling period, the observer estimates the current at the $k+1$ moment. According to the analysis in the previous section, the estimated current can rapidly converge to the actual current. Therefore, (27) can be rewritten as

$$\hat{\breve{x}}^{r}_{[k+2]} = \hat{\breve{x}}_{[k+1]} + \left(\breve{\boldsymbol{A}}\hat{\breve{x}}_{[k+1]} + \breve{\boldsymbol{B}}u_{[k+1]}\right)(T_s + hT_s). \tag{28}$$

The improved discrete DPCC algorithm is shown in Fig. 6.

C. DPCC Method With Extended State Observer

Based on the discretization DPCC model and considering the practical application, the cost function can be defined as

$$\bar{g} = \left(\breve{x}^* - \hat{\breve{x}}^{r}_{[k+2]}\right)^T\left(\breve{x}^* - \hat{\breve{x}}^{r}_{[k+2]}\right). \tag{29}$$

Differentiating the cost function and solving the minimum value of the voltage vector $u_{[k+1]}$, so the control voltage applied to the motor can be expressed as

$$u_{[k+1]} = \breve{\boldsymbol{B}}^{-1}\left\{\breve{x}^* - [\hat{\breve{x}}_{[k+1]} + \breve{\boldsymbol{A}}\hat{\breve{x}}_{[k+1]}(T_s + hT_s)]\right\}/(T_s + hT_s) \tag{30}$$

$$\left|u_{[k+1]}\right| \le u_{\max}. \tag{31}$$

In accordance with the analysis in the preceding section, the improved discretized ESO is merged with DPCC, and the control block diagram of the system is shown in Fig. 7.

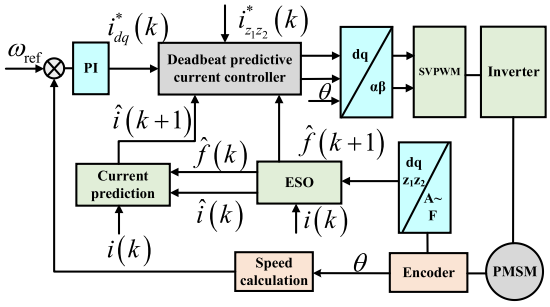

Fig. 7. Diagram of the proposed DPCC algorithm with ESO.

According to (28), the state-space equation is expanded, and DPCC with ESO can be expressed as

$$\begin{bmatrix}\hat{i}_{[k+1]}\\ \hat{d}_{[k+1]}\end{bmatrix} = \begin{bmatrix}\hat{i}_{[k]}\\ \hat{d}_{[k]}\end{bmatrix} + \left(\begin{bmatrix}\boldsymbol{A} & \boldsymbol{I}\\ 0 & 0\end{bmatrix}\begin{bmatrix}\hat{i}_{[k]}\\ \hat{d}_{[k]}\end{bmatrix} + \begin{bmatrix}\boldsymbol{B}\\ 0\end{bmatrix} u_{[k]} + K\boldsymbol{L}\begin{bmatrix}C & 0\end{bmatrix}\begin{bmatrix}i_{[k]}-\hat{i}_{[k]}\\ d_{[k]}-\hat{d}_{[k]}\end{bmatrix}\right) T_s. \tag{32}$$

According to (30) and (32), the deadbeat predicted current control of DTP-PMSM with lumped disturbance compensation combined with ESO can be expressed as

$$u_{[k+1]} = \boldsymbol{B}^{-1}\{i^* - [\hat{i}_{[k+1]} + (\boldsymbol{A}\hat{i}_{[k+1]} + \hat{d}_{[k+1]})(T_s + hT_s)]\}/(T_s + hT_s). \tag{33}$$

In this section, the designed observer is discretized and combined with DPCC. The control scheme of DTP-PMSM consists of ESO and a deadbeat controller. By adding ESO to the predictive current control algorithm, the impact of parameter mismatch and delay will be greatly reduced, and the system's robustness will be improved.

D. Stability Analysis

For the proposed ESO, when the observer's gain changes with the adjustable factor *K*, the characteristic (18) can be rewritten as

$$\left|s\boldsymbol{I} - \left(\breve{\boldsymbol{A}} - K\boldsymbol{L}\breve{\boldsymbol{C}}\right)\right| = a_4 s^4 + a_3 s^3 + a_2 s^2 + a_1 s^2 + a_0 \tag{34}$$

where

$$\begin{aligned} &a_4 = 1, a_3 = b_1 + b_2 > 0\\ &a_2 = \omega_e^2 + b_1 b_2 + k^2 l_3 + k^2 l_4 > 0\\ &a_1 = b_1 k^2 l_4 + b_2 k^2 l_3 > 0, a_0 = k^4 l_3 l_4 > 0\\ &b_1 = R_s/L_d + k l_1 > 0, b_2 = R_s/L_q + k l_2 > 0. \end{aligned} \tag{35}$$

The Hurwitz array can be expressed as

$$\Delta = \begin{bmatrix} a_3 & a_1 & 0 & 0\\ a_4 & a_2 & a_0 & 0\\ 0 & a_3 & a_1 & 0\\ 0 & a_4 & a_2 & a_0 \end{bmatrix}. \tag{36}$$

According to Hurwitz stability criterion, the sufficient and necessary condition for system stability is that all order main subformulas of the component determinant of (36) are greater than zero, which can be expressed as

$$\begin{aligned} &\Delta_1 = a_3 > 0\\ &\Delta_2 = a_3\left(\omega_e^2 + b_1 b_2\right) + b_1 k^2 l_3 + b_2 k^2 l_4 > 0\\ &\Delta_3 = a_1 a_3\left(\omega_e^2 + b_1 b_2\right) + b_1 b_2\left(k^2 l_3 - k^2 l_4\right)^2 > 0\\ &\Delta_4 = a_0\Delta_3 + a_1 a_2 a_3 a_4 > 0. \end{aligned} \tag{37}$$

Therefore, the system can remain stable when the designed observer parameters satisfy the requirements in (37).

Lyapunov criterion can further prove the stability of the proposed ESO. According to (33), the discrete-time Lyapunov function can be expressed as

$$V_{[k]} = \frac{1}{2}\left(\breve{x}^* - \hat{\breve{x}}^r_{[k+2]}\right)^T\left(\breve{x}^* - \hat{\breve{x}}^r_{[k+2]}\right). \tag{38}$$

Its difference function can be expressed as

$$\begin{aligned}\Delta V &= V_{[k+1]} - V_{[k]}\\ &= -\left(2\breve{x}^* - \hat{\breve{x}}^r_{[k+3]} - \hat{\breve{x}}^r_{[k+2]}\right)^T\left(\hat{\breve{x}}^r_{[k+3]} - \hat{\breve{x}}^r_{[k+2]}\right).\end{aligned} \tag{39}$$

It can be seen from (30), when the system constraint $u_{\lim}$ is satisfied, $V_{[k]} = 0$ and $\Delta V = 0$ can be always maintained. Therefore, the system can achieve Lyapunov stability.

Considering the existence of external disturbance and other factors, the system constraints may not be satisfied under harsh working conditions. The system condition changes to

$$\hat{\breve{x}}^r_{[k+2]} > 0 V_{[k]} > 0 \tag{40}$$

and

$$\begin{aligned} &u_{[k+1]} < -u_{\lim} u_{[k+2]} < -u_{\lim}\\ \text{or}\quad &u_{[k+1]} > u_{\lim} u_{[k+2]} > u_{\lim}. \end{aligned} \tag{41}$$

Take the condition $u_{[k+1]}$ for example, according to (28), it obtains

$$\begin{aligned}\breve{x}^* = \hat{\breve{x}}^r_{[k+2]}\left(u_{[k+1]}\right) &= \hat{\breve{x}}_{[k+1]} + \left(\breve{\boldsymbol{A}}\hat{\breve{x}}_{[k+1]} + \breve{\boldsymbol{B}}u_{[k+1]}\right)(T_s + hT_s)\\ &< \hat{\breve{x}}^r_{[k+2]}\left(-u_{\lim}\right) = \hat{\breve{x}}_{[k+1]} + \left(\breve{\boldsymbol{A}}\hat{\breve{x}}_{[k+1]} + \breve{\boldsymbol{B}}u_{[k+1]}\right)(T_s + hT_s) \Rightarrow \breve{x}^* - \hat{\breve{x}}^r_{[k+2]}\left(-u_{\lim}\right) < 0.\end{aligned} \tag{42}$$

Obviously, similar conclusions can be drawn for the other cases in (41). Therefore, the difference (39) can be further derived as

$$\Delta V = -\left(2\breve{x}^* - \hat{\breve{x}}^r_{[k+3]} - \hat{\breve{x}}^r_{[k+2]}\right)^T\left[\boldsymbol{I} + \breve{\boldsymbol{A}}(T_s + hT_s)\right]\left(\hat{\breve{x}}^r_{[k+2]} - \hat{\breve{x}}^r_{[k+1]}\right). \tag{43}$$

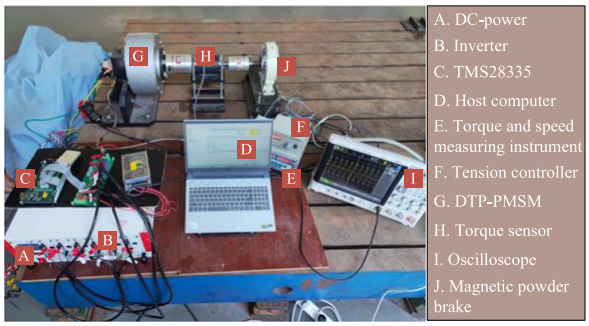

Fig. 8. Test platform for the proposed DPCC method.

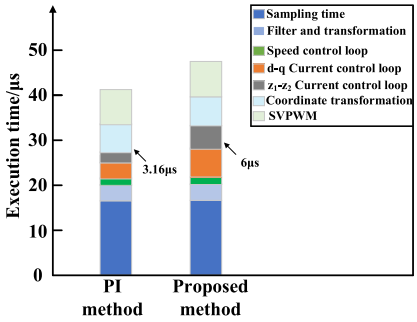

Fig. 9. Comparison of execution time with different control methods.

At this time, for the output variables under different system constraints, one can have

$$x_{[k+2]} < x_{[k+1]}, \hat{\overset{.}{x}}_{[k+2]} < \hat{\overset{.}{x}}_{[k+1]} \left(u_{input} < -u_{\lim}\right)$$
$$x_{[k+2]} > x_{[k+1]}, \hat{\overset{.}{x}}_{[k+2]} > \hat{\overset{.}{x}}_{[k+1]} \left(u_{input} > -u_{\lim}\right). \quad (44)$$

Therefore, according to (44), even when the system constraint is exceeded, there is still

$$V_{[k]} > 0, \Delta V < 0. \quad (45)$$

According to Lyapunov theorem, the proposed control system can achieve stability.

V. Experimental Results and Analysis

A. Experimental Parameter

The proposed DPCC control method with ESO and the conventional DPCC control method are applied respectively in an experiment to test the system's effectiveness. Table I lists the specific parameters of the motor used in the experiment. The extended state observation gains are selected as $\lambda = 400$, $\xi = 0.4\pi$.

The test platform used in the experiment is shown in Fig. 8, which mainly includes an experimental DTP-PMSM, a TMS320F28335 digital signal processor, and a PC to monitor and analyze the collected experimental data. In the experiment, the maximum CPU frequency of the controller was 150 MHz, and the sampling frequency is selected as 20 KHz.

Fig. 9 shows the comparison between PI control and the number of executions of the proposed method in different stages.

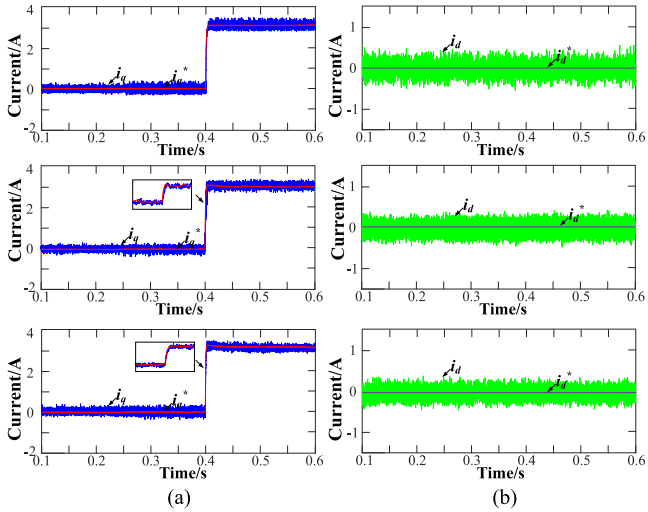

Fig. 10. Comparison of current response with the step load under the L_{dq} mismatch ($\tilde{L}_d = 0.5L_d$, $\tilde{L}_q = 0.5L_q$). (a) q-axis current. (b) d-axis current.

In the experiment, TMS320F28335 single-chip microcomputer is used as the executive element of different control methods. The sampling period of the controller in this article is 50 μs. In most cases, the execution time of the two controls is similar. The difference is mainly generated in the current control loop. A total of 6 μs is needed to process the proposed DPCC, which is substantially more than the 3 μs that is needed for conventional PI control. From the perspective of the overall execution time, the proposed control strategy is not much different from the PI control, which is 47.3 μs, while the conventional PI control is 41.3 μs. Since the controller's sampling period is 50 μs, both can be implemented in one sampling period.

Overall, the proposed approach would take more time to implement but would not impact overall control.

To further explore the proposed DPCC's control performance in parameter mismatch, a series of experiments are conducted under various operating settings of the DTP-PMSM. Considering that the effect caused by stator resistance mismatch is small and can be ignored in practice, the experiment only studies the current response when the inductance and flux linkage are mismatched. Notably, the current waveforms of three different control methods are compared under each experimental condition. In the subsequent figures, the waveforms from top to bottom are obtained from conventional DPCC, the improved DPCC strategy based on a composite observer including GPIO and SMO [29], and the proposed ESO-based DPCC strategy, respectively.

B. Comparison of the Control Performance Under the Step Load Condition

To further analyze the control performance of the proposed DPCC under given system parameter variations, the current response of different control schemes under motor parameter mismatch is compared using experiments. Figs. 10–15 show the current responses of d-q axis when the flux and inductance of

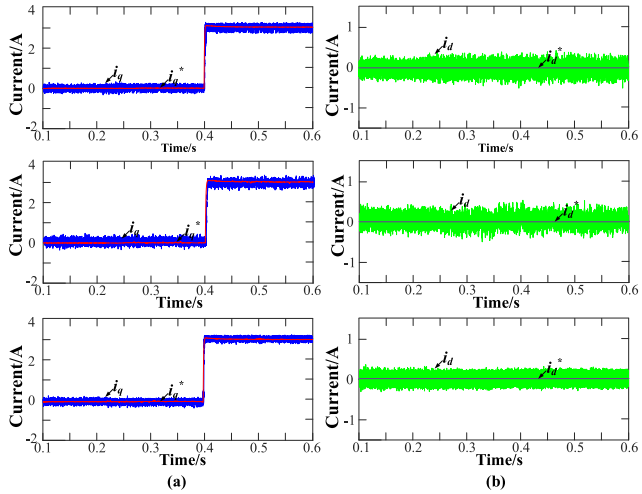

Fig. 11. Comparison of current response with the step load under the L_{dq} mismatch ($\tilde{L}_d = 2L_d$, $\tilde{L}_q = 2L_q$). (a) q-axis current. (b) d-axis current.

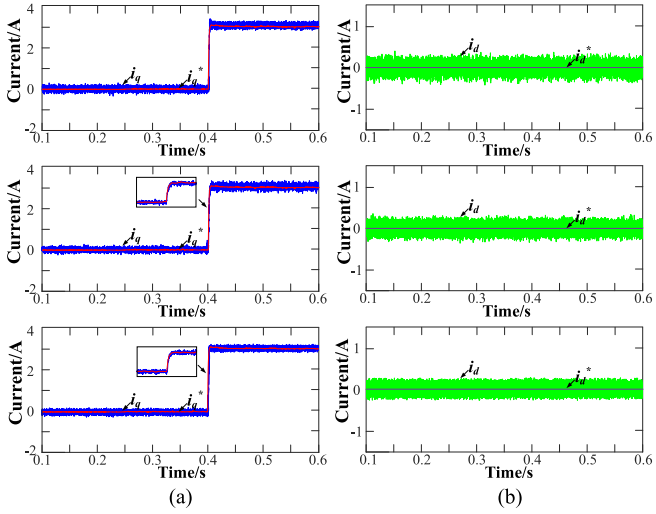

Fig. 12. Comparison of current response of the conventional DPCC and proposed DPCC with the step load under the ψ_f mismatch ($\tilde{\varphi}_f = 0.5\varphi_f$). (a) q-axis current. (b) d-axis current.

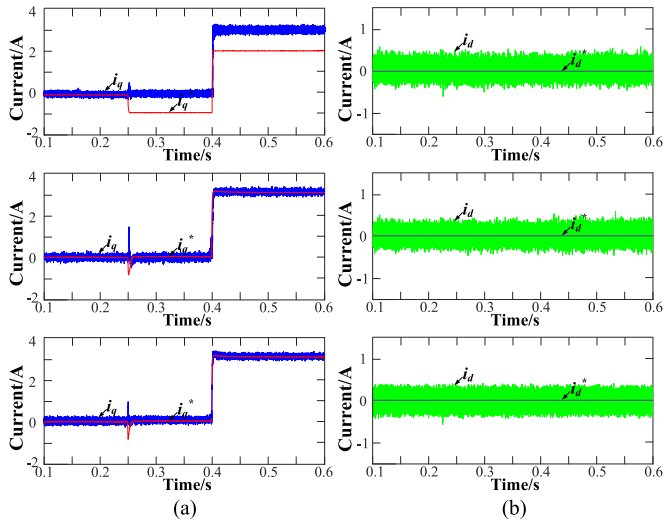

Fig. 13. Comparison of current response with the step load under the ψ_f mismatch ($\tilde{\varphi}_f = 2\varphi_f$). (a) q-axis current. (b) d-axis current.

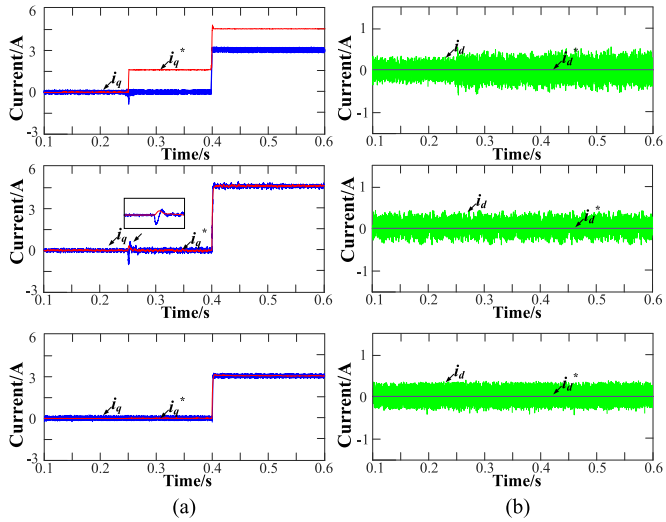

Fig. 14. Comparison of current response with the step load under the L_{dq} and ψ_f mismatch ($\tilde{L}_d = 0.5L_d$, $\tilde{L}_q = 0.5L_q$, $\tilde{\varphi}_f = 0.5\varphi_f$). (a) q-axis current. (b) d-axis current.

the motor deviate from the calibrated values, respectively. The reference speed of DTP-PMSM is 400 r/min, and the load torque changes from 0 to 50 N·m at 0.4 s.

Figs. 10 and 11 show the comparison of d-q axis current when inductance changes, respectively. L_{dq} mutated to 0.5 and 2 times of the calibration value at 0.25 s, respectively. As can be seen from Figs. 10 and 11, when the inductance mismatch happens, the current response under the control of conventional DPCC produces a large current ripple. The DPCC based on composite observer has longer response time and larger overshoot during the torque's step change. Under the same operating conditions, the proposed DPCC compensates the voltage by means of a disturbance observer, improving the current waveform.

Similarly, Figs. 12 and 13 compare d-q axis currents under different control schemes when the flux linkage fluctuates. According to the sensitivity analysis of the motor parameters in the previous section, when the flux linkage is disturbed, the impact on the motor mainly focuses on the current response of the q-axis. As shown in Fig. 13(a), as the actual magnetic flux rises to two times the calibrated value, a steady-state error with a peak value of 1.1 A occurs for the q-axis current under conventional DPCC control. As can be seen from Figs. 12 and 13, regardless of the magnitude of the magnetic linkage error, the current response of the d-q axis under DPCC control in this article can always well track the reference value, and the steady-state error remains around 0. Although the composite observe-based DPCC also eliminates steady-state errors, the proposed scheme has better performance in terms of both overshoot and response time.

Figs. 14 and 15 show the comparison of d-q axis currents of different control strategies when the inductance and magnetic

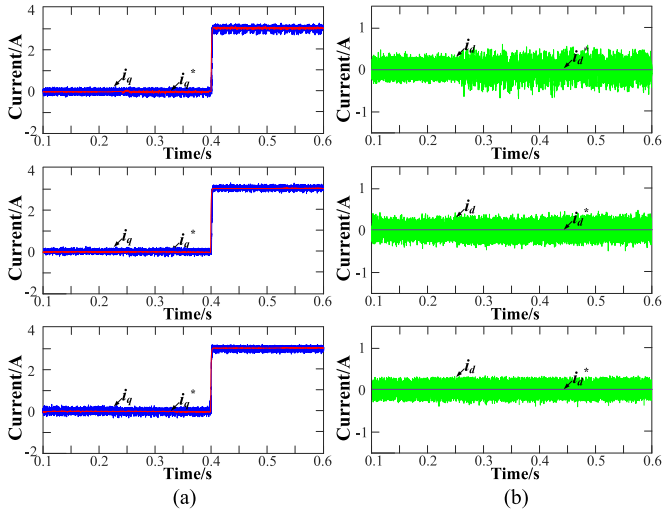

Fig. 15. Comparison of current response with the step load under the L_{dq} and ψ_f mismatch ($\tilde{L}_d = 2L_d$, $\tilde{L}_q = 2L_q$, $\tilde{\varphi}_f = 2\varphi_f$). (a) q-axis current. (b) d-axis current.

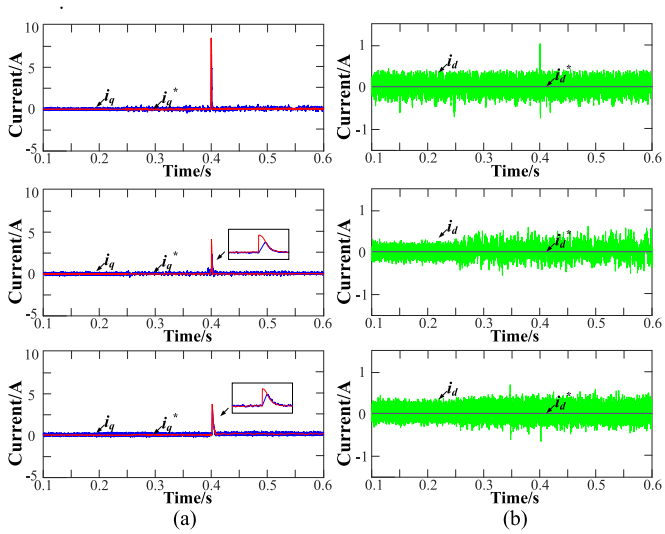

Fig. 16. Comparison of current response with the step speed under the L_{dq} mismatch ($\tilde{L}_d = 0.5L_d$, $\tilde{L}_q = 0.5L_q$). (a) q-axis current. (b) d-axis current.

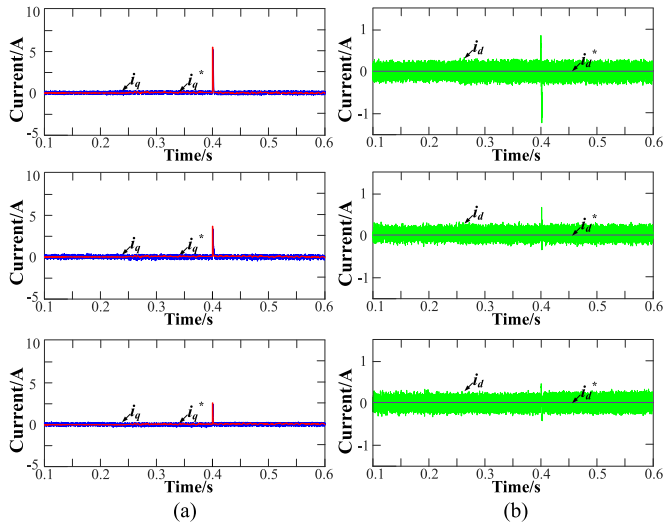

Fig. 17. Comparison of current response with the step speed under the L_{dq} mismatch ($\tilde{L}_d = 2L_d$, $\tilde{L}_q = 2L_q$). (a) q-axis current. (b) d-axis current.

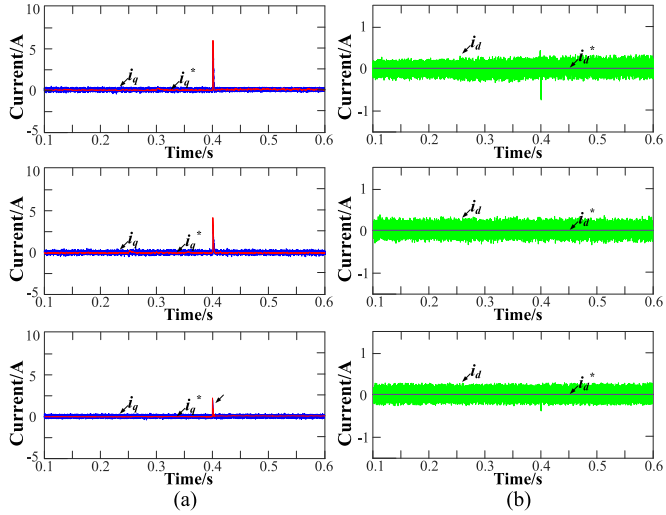

Fig. 18. Comparison of current response with the step speed under the ψ_f mismatch ($\tilde{\varphi}_f = 0.5\varphi_f$). (a) q-axis current. (b) d-axis current.

linkage vary simultaneously. The proposed DPCC has significantly decreased the current ripple compared to the conventional method. At the same time, as can be seen from Fig. 14, the current of the DPCC based on the composite observer fluctuates greatly, resulting in a temporary steady-state error. While the proposed DPCC completely eliminates the steady-state error of the current of q-axis with a peak value of 1.5 A through compensation, improving control accuracy and robustness.

C. Comparison of the Control Performance Under the Step Speed Condition

Figs. 16–21 compares the current response of the different schemes when the rotational speed reference of a no-load motor changes under different parameter mismatches. Before 0.25 s, the motor was operating at a stable operating condition of 400 r/min with accurate parameters. At 0.25 s, the motor parameters change differently. At 0.4 s, the reference speed of the motor steps to 420 r/min under parameter mismatch.

As can be seen from Figs. 16 and 17, the proposed DPCC significantly reduces the peak current in the system response when the rotational speed undergoes a sudden change, which is only one-third of that of a conventional DPCC. At the same time, the steady-state current of DPCC with ESO is more stable, and the steady-state error is almost maintained at 0.

The experimental results of a step change in rotational speed due to a mismatch in the magnetic linkage are shown in Figs. 18 and 19, respectively. Compared to other DPCC schemes, the proposed DPCC greatly improves current overshoot caused by speed steps, reduces the time for the system to reach a steady

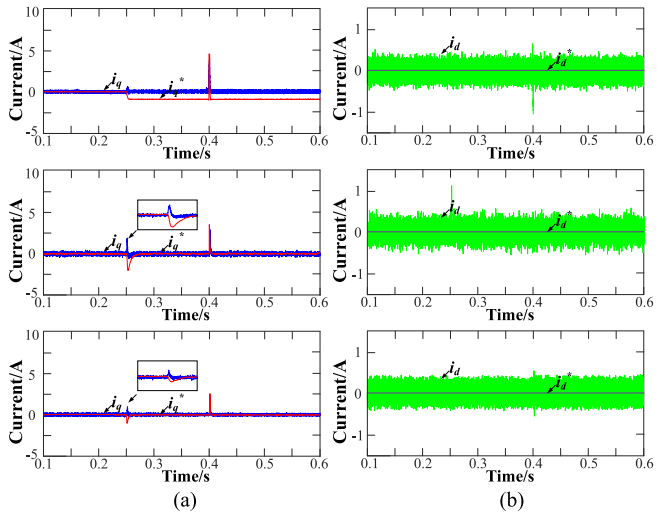

Fig. 19. Comparison of current response with the step speed under the ψ_f mismatch ($\tilde{\varphi}_f = 2\varphi_f$). (a) q-axis current. (b) d-axis current.

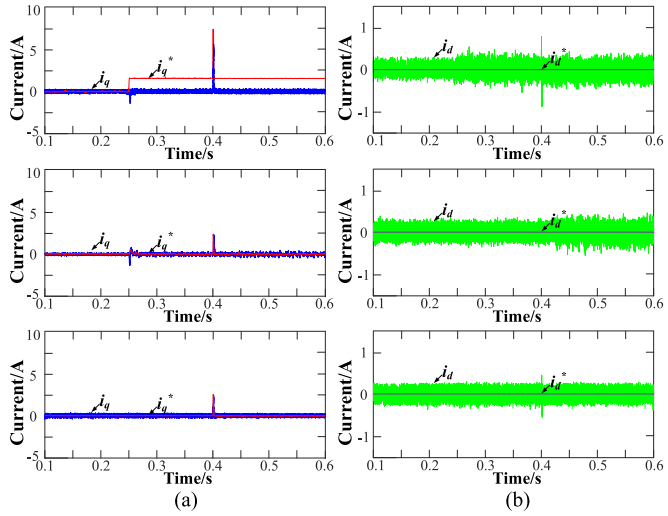

Fig. 20. Comparison of current response with the step speed under the L_{dq} and ψ_f mismatch ($\tilde{L}_d = 0.5L_d$, $\tilde{L}_q = 0.5L_q$, $\tilde{\varphi}_f = 0.5\varphi_f$). (a) q-axis current. (b) d-axis current.

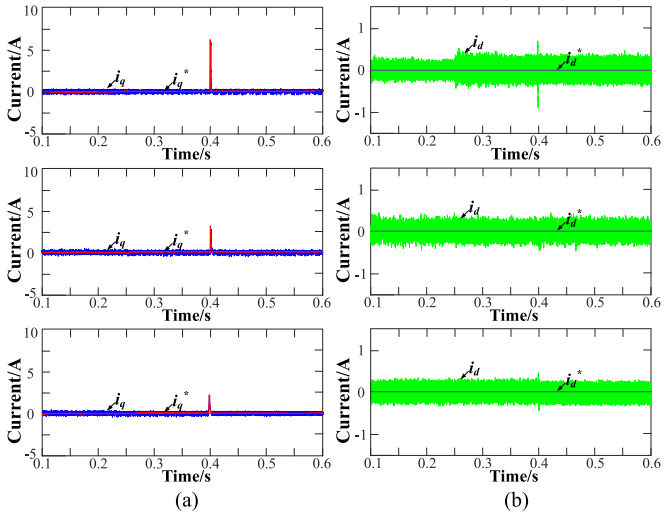

Fig. 21. Comparison of current response with the step speed under the L_{dq} and ψ_f mismatch ($\tilde{L}_d = 2$, $\tilde{L}_q = 2L_q$, $\tilde{\varphi}_f = 2\varphi_f$). (a) q-axis current. (b) d-axis current.

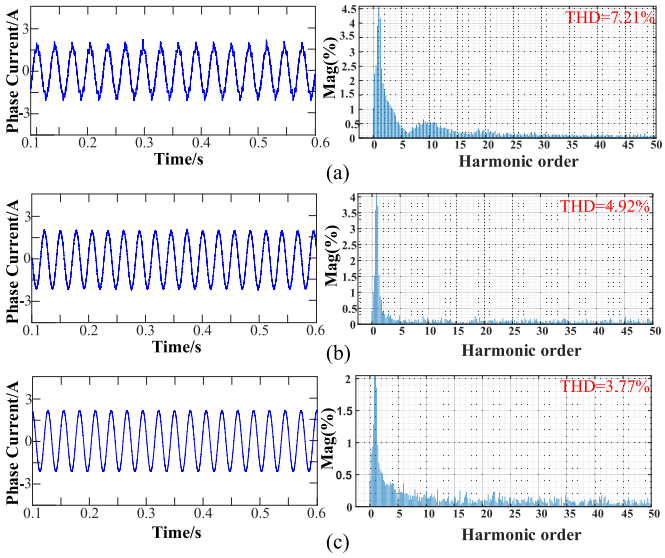

Fig. 22. Comparison of phase-current and FFT analysis with different control methods. (a) PI control. (b) Conventional DPCC. (c) Proposed DPCC.

state, and improves transient control performance. As shown in Fig. 19, in a conventional DPCC strategy, the q-axis current response produces a steady-state error of about 1.5 A, which prevents accurate tracking of the reference current. By adding observer compensation, the error is quickly eliminated after a short delay, effectively improving the control performance of the system.

Figs. 20 and 21 show the current response when the magnetic linkage and torque simultaneously deviate from the calibration value. Under experimental conditions, the current response of the conventional DPCC strategy has lost its ability to track the reference current. Although the disturbance is compensated, the poor dynamic performance and large current ripple of DPCC based on composite observer cannot be ignored under parameter mismatch. In contrast, the control indicators of the proposed DPCC have been significantly improved, eliminating steady-state errors in a relatively short time and optimizing the current waveform.

D. Comparison of the Conventional DPCC and Proposed DPCC in Harmonic Suppression

In order to verify the performance of the proposed control method in suppressing harmonics, the current waveforms under three different methods are compared in the experiment. The experimental reference speed is set to 400 r/min, and the load torque is 50 N·m. At the same time, the parameters of the motor are set to 0.5 times the calibration value to simulate the parameter mismatch.

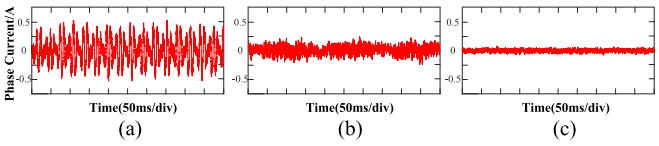

Fig. 23. Comparison of current in z_1-z_2 axis with different control methods. (a) PI control. (b) Conventional DPCC. (c) Proposed DPCC.

Fig. 22 shows the phase current waveforms and FFT analysis results of three different control methods. Compared with the conventional DPCC and PI control strategies, the proposed DPCC strategy basically eliminates the distortion that occurs at the peak of the current, while also avoiding the peak at the top of the waveform. The sinusoidal waveform of the phase current has significantly improved.

As shown in Fig. 22, the fifth and seventh harmonics of DPCC are significantly reduced. The proposed DPCC has lower total harmonic distortion and better overall harmonic suppression performance.

Considering that the fifth and seventh harmonics of the proposed DTP-PMSM are mainly generated in z_1-z_2 subspace, the main mean of suppressing harmonics is to control the current in z_1-z_2 subspace, so direct analysis of the current waveform of i_z can better verify the performance of harmonic suppression. As can be seen from Fig. 23, the peak current of conventional DPCC is as high as 0.6 A, while the peak under the proposed DPCC is only about 0.1 A. At the same time, the jitter of the current waveform is well controlled and becomes smoother.

Therefore, the proposed control method significantly improves suppressing harmonic manifestations.

E. Comparison of Observer Estimation Performance

In order to further verify the superiority of the proposed ESO in estimating performance, the disturbance compensation of the proposed ESO under parameter mismatch is compared with that of the conventional ESO in this section. In the experiment, the load torque is set to 50 N·m and the speed is set to 400 r/min. The resistance R_s, inductance L_d and L_q, and flux ψ_f of the motor will deviate from the calibration value in 0.3 s, respectively.

As shown in Fig. 24, although both observers can respond quickly and compensate the *dq* axis error at 0.3 s, compared with the conventional scheme, the disturbance estimate ripple of the proposed scheme is greatly reduced when compensating for parameter mismatch disturbance. This phenomenon is particularly obvious when the flux fluctuates. The estimated disturbances d_d and d_q of the proposed scheme are reduced from 27.3541 V and 17.9721 V to 21.3624 V and 13.5813 V by 28% and 32%, respectively. Similar conclusions are also obtained under other working conditions. This proves that the proposed ESO has better buffeting performance.

In summary, the proposed ESO achieves more stable compensation performance and robustness under parameter mismatch due to the addition of adaptive parameters.

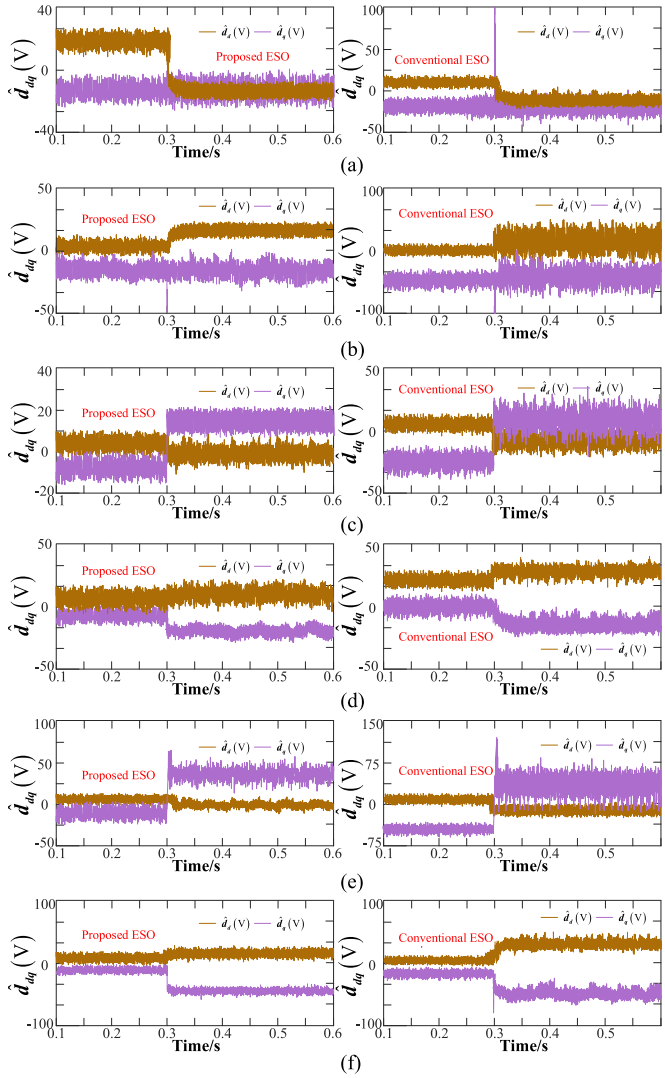

Fig. 24. Comparison of disturbances estimated by proposed ESO and conventional ESO. (a) $\tilde{L}_d = 0.5L_d$, $\tilde{L}_q = 0.5L_q$. (b) $\tilde{L}_d = 2L_d$, $\tilde{L}_q = 2L_q$. (c) $\tilde{\varphi}_f = 0.5\varphi_f$. (d) $\tilde{\varphi}_f = 2\varphi_f$. (e) $\tilde{L}_d = 0.5L_d, \tilde{L}_q = 0.5L_q$, $\tilde{\varphi}_f = 0.5\varphi_f$. (f) $\tilde{L}_d = 2$, $\tilde{L}_q = 2L_q$, $\tilde{\varphi}_f = 2\varphi_f$.

VI. Conclusion

A DPCC control method based on variable gain ESO is proposed to solve the disturbance problem in the process of DTP-PMSM operation. Considering the inherent delay in conventional DPCC, an optimized prediction model is designed to further eliminate the delay effect caused by inductors, sensors, etc. The proposed strategy improves the control performance and has better robustness when the motor parameters are mismatched. The application of the strategy in harmonic subspace also further eliminates the effects of fifth and seventh harmonics. Compared with other observers, the exponential variable gain ESO accelerates the convergence rate of the observer. By estimating and compensating current loop disturbance quickly and efficiently, the observer can improve the control accuracy and response time of the system, especially in the case of variable system parameters. At the same time, the ESO-based DPCC

proposed in this article has fewer adjustment parameters, strong robustness, and can better adapt to complex and variable working conditions, and improve the typical harmonic problems in the operation of DTP-PMSM. The experimental results support the feasibility of DTP-PMSM and the superiority of the proposed DPCC and observer.

REFERENCE

[1] E. Levi, F. Barrero, and M. J. Duran, "Multiphase machines and drives—revisited," *IEEE Trans. Ind. Electron.*, vol. 63, no. 1, pp. 429–432, Jan. 2016.

[2] X. Sun, Z. Shi, G. Lei, Y. Guo, and J. Zhu, "Multi-objective design optimization of an IPMSM based on multilevel strategy," *IEEE Trans. Ind. Electron.*, vol. 68, no. 1, pp. 139–148, Jan. 2021.

[3] F. J. Anayi and M. M. A. Al Ibraheemi, "Estimation of rotor position for permanent magnet synchronous motor at standstill using sensorless voltage control scheme," *IEEE/ASME Trans. Mechatronics*, vol. 25, no. 3, pp. 1612–1621, Jun. 2020.

[4] X. Sun, N. Xu, and M. Yao, "Sequential subspace optimization design of a dual three-phase permanent magnet synchronous hub motor based on NSGA III," *IEEE Trans. Transp. Electrific.*, vol. 9, no. 1, pp. 622–630, Mar. 2023.

[5] G. Rezazadeh, F. Tahami, G.-A. Capolino, Z. Nasiri-Gheidari, H. Henao, and M. Sahebazamani, "Improved design of a six-phase squirrel cage induction motor with pseudo-concentrated windings," *IEEE J. Emerg. Sel. Topics Ind. Electron.*, vol. 3, no. 4, pp. 1187–1194, Oct. 2022.

[6] Z. Jin, X. Sun, G. Lei, Y. Guo, and J. Zhu, "Sliding mode direct torque control of SPMSMs based on a hybrid wolf optimization algorithm," *IEEE Trans. Ind. Electron.*, vol. 69, no. 5, pp. 4534–4544, May 2022.

[7] M. S. Rafaq and J.-W. Jung, "A comprehensive review of state-of-the-art parameter estimation techniques for permanent magnet synchronous motors in wide speed range," *IEEE Trans. Ind. Inform.*, vol. 16, no. 7, pp. 4747–4758, Jul. 2020.

[8] X. Sun, Z. Su, G. Lei, and M. Yao, "Robust predictive cascaded speed and current control for PMSM drives considering parameter variations," *IEEE Trans. Ind. Electron.*, to be published, doi: 10.1109/TIE.2023.3337498.

[9] B. Zheng, J. Zou, B. Li, M. Tang, Y. Xu, and P. Zanchetta, "Analysis and fault-tolerant control for dual-three-phase PMSM based on virtual healthy model," *IEEE Trans. Power Electron.*, vol. 37, no. 12, pp. 15411–15424, Dec. 2022.

[10] M. Gu, Z. Wang, and O. Dordevic, "Analysis and reduction of current and voltage ripple in DC link for three-level NPC inverter-fed dual three-phase motor drives," *IEEE Trans. Power Electron.*, vol. 38, no. 4, pp. 5128–5140, Apr. 2023.

[11] Z. Su, X. Sun, G. Lei, and M. Yao, "Model-free predictive current control for dual three-phase PMSM drives with an optimal modulation pattern," *IEEE Trans. Ind. Electron.*, to be published, doi: 10.1109/TIE.2023.3327554.

[12] S. Liu, Z. Song, Y. Liu, Y. Chen, and C. Liu, "Flux-weakening controller design of dual three-phase PMSM drive system with copper loss minimization," *IEEE Trans. Power Electron.*, vol. 38, no. 2, pp. 2351–2363, Feb. 2023.

[13] S. Hu, Z. Liang, W. Zhang, and X. He, "Research on the integration of hybrid energy storage system and dual three-phase PMSM drive in EV," *IEEE Trans. Ind. Electron.*, vol. 65, no. 8, pp. 6602–6611, Aug. 2018.

[14] K. Yu, Z. Wang, M. Gu, and X. Wang, "Universal control scheme of dual three-phase PMSM drives with single open-phase fault," *IEEE Trans. Power Electron.*, vol. 37, no. 12, pp. 14034–14039, Dec. 2022.

[15] K. Eshwar and V. K. Thippiripati, "Weighting-factorless predictive torque control scheme for dual inverter fed open-end-winding PMSM with single DC source," *IEEE Trans. Power Electron.*, vol. 36, no. 11, pp. 12968–12978, Nov. 2021.

[16] X. Sun, T. Li, M. Yao, G. Lei, Y. Guo, and J. Zhu, "Improved finite-control-set model predictive control with virtual vectors for PMSHM drives," *IEEE Trans. Energy Convers.*, vol. 37, no. 3, pp. 1885–1894, Sep. 2022.

[17] Y. Luo and C. Liu, "A simplified model predictive control for a dual three-phase PMSM with reduced harmonic currents," *IEEE Trans. Ind. Electron.*, vol. 65, no. 11, pp. 9079–9089, Nov. 2018.

[18] X. Sun, Y. Zhang, Y. Cai, and X. Tian, "Compensated deadbeat predictive current control considering disturbance and VSI nonlinearity for in-wheel PMSMs," *IEEE/ASME Trans. Mechatronics*, vol. 27, no. 5, pp. 3536–3547, Oct. 2022.

[19] W. Wang, C. Liu, S. Liu, and H. Zhao, "Model predictive torque control for dual three-phase PMSMs with simplified deadbeat solution and discrete space-vector modulation," *IEEE Trans. Energy Convers.*, vol. 36, no. 2, pp. 1491–1499, Jun. 2021.

[20] C. Xu, Z. Han, and S. Lu, "Deadbeat predictive current control for permanent magnet synchronous machines with closed-form error compensation," *IEEE Trans. Power Electron.*, vol. 35, no. 5, pp. 5018–5030, May 2020.

[21] I. Harbi, M. Ahmed, M. L. Heldwein, R. Kennel, and M. Abdelrahem, "Enhanced fault-tolerant robust deadbeat predictive control for nine-level ANPC-based converter," *IEEE Access*, vol. 10, pp. 108492–108505, 2022.

[22] K. Yu, Z. Wang, W. Hua, and M. Cheng, "Robust cascaded deadbeat predictive control for dual three-phase variable-flux PMSM considering intrinsic delay in speed loop," *IEEE Trans. Ind. Electron.*, vol. 69, no. 12, pp. 12107–12118, Dec. 2022.

[23] T. Li, X. Sun, G. Lei, Y. Guo, Z. Yang, and J. Zhu, "Finite-control-set model predictive control of permanent magnet synchronous motor drive systems - an overview," *IEEE/CAA J. Automatica Sinica*, vol. 9, no. 12, pp. 2087–2105, Dec. 2022.

[24] S. Liu and C. Liu, "Direct harmonic current control scheme for dual three-phase PMSM drive system," *IEEE Trans. Power Electron.*, vol. 36, no. 10, pp. 11647–11657, Oct. 2021.

[25] X. Sun, Y. Zhang, G. Lei, Y. Guo, and J. Zhu, "An improved deadbeat predictive stator flux control with reduced-order disturbance observer for in-wheel PMSMs," *IEEE/ASME Trans. Mechatronics*, vol. 27, no. 2, pp. 690–700, Apr. 2022.

[26] Y. Han, S. Chen, C. Gong, X. Zhao, F. Zhang, and Y. Li, "Accurate SM disturbance observer-based demagnetization fault diagnosis with parameter mismatch impacts eliminated for IPM motors," *IEEE Trans. Power Electron.*, vol. 38, no. 5, pp. 5706–5710, May 2023.

[27] Y. Lu, T. Cao, W. G. Ge, Y. Zhao, and G. Wang, "Adaptive disturbance observer-based improved super-twisting sliding mode control for electromagnetic direct-drive pump," *Smart Mater. Struct.*, vol. 32, no. 1, Dec. 2023, Art. no. 17001.

[28] T. Li, X. Sun, M. Yao, D. Guo, and Y. Sun, "Improved finite control set model predictive current control for permanent magnet synchronous motor with sliding mode observer," *IEEE Trans. Transp. Electrific.*, to be published, doi: 10.1109/TTE.2023.3293510.

[29] K. Yu and Z. Wang, "Improved deadbeat predictive current control of dual three-phase variable-flux PMSM drives with composite disturbance observer," *IEEE Trans. Power Electron.*, vol. 37, no. 7, pp. 8310–8321, Jul. 2022.

[30] W. Wang, C. Liu, Z. Song, and Z. Dong, "Harmonic current suppression for dual three-phase PMSM based on deadbeat control and disturbance observer," *IEEE Trans. Ind. Electron.*, vol. 70, no. 4, pp. 3482–3492, Apr. 2023.

[31] L. Wang, J. Zhao, X. Yang, Z. Zheng, X. Zhang, and L. Wang, "Robust deadbeat predictive current regulation for permanent magnet synchronous linear motor drivers with parallel parameter disturbance and load observer," *IEEE Trans. Power Electron.*, vol. 37, no. 7, pp. 7834–7845, Jul. 2022.

[32] X. Sun, T. Li, X. Tian, and J. Zhu, "Fault-tolerant operation of a six-phase permanent magnet synchronous hub motor based on model predictive current control with virtual voltage vectors," *IEEE Trans. Energy Convers.*, vol. 37, no. 1, pp. 337–346, Mar. 2022.

[33] S. Xu et al., "A reduced-order observer-based method for simultaneous diagnosis of open-switch and current sensor faults of a grid-tied NPC inverter," *IEEE Trans. Power Electron.*, vol. 38, no. 7, pp. 9019–9032, Jul. 2023.

[34] B. Guo, S. Bacha, M. Alamir, A. Hably, and C. Boudinet, "Generalized integrator-extended state observer with applications to grid-connected converters in the presence of disturbances," *Trans. Control Syst. Technol.*, vol. 29, no. 2, pp. 744–755, Mar. 2021.

[35] Z. Hao, Y. Yang, K. Shao, and Y. Liu, "Switching active disturbance rejection based deadbeat predictive current control for permanent magnet synchronous motors," *IEEE Trans. Power Electron.*, vol. 38, no. 11, pp. 13920–13932, Nov. 2023.

[36] T. Wang, G. Luo, Z. Chen, W. Tu, and C. Liu, "An improved robust model predictive speed control with inertia identification for PMSM drives in the electrohydrostatic actuator," *IEEE Trans. Power Electron.*, vol. 38, no. 11, pp. 13825–13841, Nov. 2023.

[37] Z. Xu, W. Deng, H. Shen, and J. Yao, "Extended-state-observer-based adaptive prescribed performance control for hydraulic systems with full-state constraints," *IEEE/ASME Trans. Mechatronics*, vol. 27, no. 6, pp. 5615–5625, Dec. 2022.

[38] S. Zhu et al., "Robust speed control of electrical drives with reduced ripple using adaptive switching high-order extended state observer," *IEEE Trans. Power Electron.*, vol. 37, no. 2, pp. 2009–2020, Feb. 2022.
[39] J. Wang, Y. Liu, J. Yang, F. Wang, and J. Rodríguez, "Adaptive integral extended state observer-based improved multistep FCS-MPCC for PMSM," *IEEE Trans. Power Electron.*, vol. 38, no. 9, pp. 11260–11276, Sep. 2023.
[40] H. Liu, W. Lin, Z. Liu, C. Buccella, and C. Cecati, "Model predictive current control with model-aid extended state observer compensation for PMSM drive," *IEEE Trans. Power Electron.*, vol. 38, no. 3, pp. 3152–3162, Mar. 2023.
[41] O. Babayomi and Z. Zhang, "Model-free predictive control of power converters with multifrequency extended state observers," *IEEE Trans. Ind. Electron.*, vol. 70, no. 11, pp. 11379–11389, Nov. 2023.
[42] X. Yang, H. Hu, H. Hu, Y. Liu, and Z. He, "A quasi-resonant extended state observer-based predictive current control strategy for three-phase PWM rectifier," *IEEE Trans. Ind. Electron.*, vol. 69, no. 12, pp. 13910–13917, Dec. 2022.

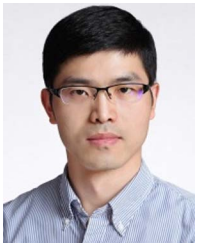

Xiaodong Sun (Senior Member, IEEE) received the B.Sc. degree in electrical engineering and the M.Sc. and Ph.D. degrees in control engineering from Jiangsu University, Zhenjiang, China, in 2004, 2008, and 2011, respectively.

Since 2004, he has been with Jiangsu University, where he is currently a Professor in vehicle engineering with the Automotive Engineering Research Institute. From 2014 to 2015, he was a Visiting Professor with the School of Electrical, Mechanical, and Mechatronic Systems, University of Technology Sydney, Sydney, Australia. His current teaching and research interests include electrified vehicles, electrical machines, electrical drives, and energy management. He is the author or coauthor of more than 100 refereed technical papers and one book, and he is the holder of 42 patents in his areas of interest.

Dr. Sun is an Associate Editor of IEEE TRANSACTIONS ON INDUSTRIAL ELECTRONICS, an Associate Editor of IEEE TRANSACTIONS ON TRANSPORTATION ELECTRIFICATION, and an Editor of IEEE TRANSACTIONS ON ENERGY CONVERSION.

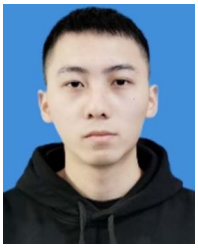

Xuwei Lin (Graduate Student Member, IEEE) was born in Taizhou, Zhejiang, China, in 2000. He received the B.S. degree in vehicle engineering from Jiangsu University, Zhenjiang, China, in 2021. He is currently working toward the M.E. degree in vehicle engineering with Jiangsu University, Zhenjiang, China.

His current research interests include predictive control for multiphase motor drives and advanced control strategy of electric machine.

Dong Guo received the B.Sc. and M.Sc. degrees in mechanical engineering from the Chongqing University of Technology, Chongqing, China, in 2007 and 2010, respectively. He received the Ph.D. degree in mechanical engineering from the Southwest Jiaotong University, Chengdu, China, in 2015.

Since 2015, he has been with Chongqing University of Technology, where he is currently a Professor in vehicle engineering and the Deputy Dean of the School of Vehicle Engineering. His current teaching and research interests include electric drive systems, intelligent cockpit systems and NVH test and analysis of driveline systems. He is the author or coauthor of more than 40 refereed technical papers and one book, and he is the holder of 16 patents and 8 software works in his areas of interest.

Dr. Guo received awards such as the China Machinery Industry Science and Technology Award, the Chongqing Science and Technology Award, and the China Automotive Engineering Society Science and Technology Award.

Gang Lei (Senior Member, IEEE) received the B.S. degree in mathematics from Huanggang Normal University, Huanggang, China, in 2003, the M.S. degree in mathematics and the Ph.D. degree in electrical engineering both from Huazhong University of Science and Technology, Wuhan, China, in 2006 and 2009, respectively.

He is currently a Senior Lecturer with the School of Electrical and Data Engineering, University of Technology Sydney (UTS), Australia. His research interests include computational electromagnetics, design optimization and control of electrical drive systems and renewable energy systems.

Dr. Lei is an Associate Editor of IEEE TRANSACTIONS ON INDUSTRIAL ELECTRONICS, an Associate Editor of IEEE TRANSACTIONS ON TRANSPORTATION ELECTRIFICATION, and an Editor of IEEE TRANSACTIONS ON ENERGY CONVERSION.

Ming Yao received the B.S. degree in vehicle engineering from Jiangsu University, Zhenjiang, China, in 2000, and the M.Sc. and Ph.D. degrees in vehicle operation engineering from Jiangsu University, Zhenjiang, China, in 2006 and 2019, respectively.

He is currently an Associate Professor with the School of Automotive and Traffic Engineering, Jiangsu University. His main research interests include electrified vehicles, vehicles' safety technology and energy saving, and environmental protection technology of vehicles.